Petroleum Science 19 (2022) 2711–2719

Contents lists available at ScienceDirect

Petroleum Science

journal homepage: www.keaipublishing.com/en/journals/petroleum-science

Original Paper

Model-data-driven P-wave impedance inversion using ResNets and the normalized zero-lag cross-correlation objective function

Yu-Hang Sun [a], Yang Liu [a, b, *]

[a] CNPC Key Laboratory of Geophysical Prospecting and State Key Laboratory of Petroleum Resources and Prospecting, China University of Petroleum (Beijing), Beijing, 102249, China
[b] China University of Petroleum (Beijing), Karamay Campus, Karamay, Xinjiang, 834000, China

ARTICLE INFO

Article history:
Received 28 December 2021
Received in revised form
21 August 2022
Accepted 14 September 2022
Available online 24 September 2022

Edited by Jie Hao

Keywords:
Model-data-driven
P-wave impedance inversion
ResNets
Zero-lag cross-correlation

ABSTRACT

Model-driven and data-driven inversions are two prominent methods for obtaining P-wave impedance, which is significant in reservoir description and identification. Based on proper initial models, most model-driven methods primarily use the limited frequency bandwidth information of seismic data and can invert P-wave impedance with high accuracy, but not high resolution. Conventional data-driven methods mainly employ the information from well-log data and can provide high-accuracy and high-resolution P-wave impedance owing to the superior nonlinear curve fitting capacity of neural networks. However, these methods require a significant number of training samples, which are frequently insufficient. To obtain P-wave impedance with both high accuracy and high resolution, we propose a model-data-driven inversion method using ResNets and the normalized zero-lag cross-correlation objective function which is effective for avoiding local minima and suppressing random noise. By using initial models and training samples, the proposed model-data-driven method can invert P-wave impedance with satisfactory accuracy and resolution. Tests on synthetic and field data demonstrate the proposed method's efficacy and practicability.

1. Introduction

P-wave impedance is a critical parameter in reservoir identification and exploration because it can indicate reservoir features. Both model-driven and data-driven inversion methods can obtain P-wave impedance from post-stack seismic data (Wang et al., 2019a; Alfarraj and AlRegib, 2019; Biswas et al., 2019; Chen and Schuster, 2020). Most model-driven methods presume that the relationship between seismic data and P-wave impedance obeys the Robinson seismic convolution model (Robinson, 1967; Dai et al., 2018; Ajaz et al., 2021; Cheng et al., 2021a). By using the Bayesian theory or series reversion theory, Robinson model-driven inversion methods update P-wave impedance models iteratively attributed to the differences between synthetic and real seismic data (Yin and Zhang, 2014; Innanen, 2011; Chen and Innanen, 2014; Hu et al., 2011; Cheng et al., 2021b). Most seismic data have limited frequency bandwidths due to acquisition constraints, but inversion targets have wide frequency bandwidths, resulting in ill-conditioned and ill-posed inversion issues (Lu et al., 2015; Kieu and Kepic, 2019; Li et al., 2020; Wang et al., 2022). As a result, model-driven methods typically necessitate well-prepared low-frequency initial models and are incapable of providing high-resolution P-wave impedance (Zhou et al., 2017, 2019; Baeten et al., 2013). Sparsity-constrained methods and well-log constrained methods are developed to supplement the missing frequency information to enhance the resolution of inverted P-wave impedance (Ma et al., 2019, 2021; Shi et al., 2020).

By using neural networks, recently developed data-driven inversion methods provide another option to achieve broad frequency bandwidth P-wave impedance (Das et al., 2019; Guo et al., 2019; Puzyrev et al., 2019; Wu et al., 2021). These methods necessitate no initial models but a significant number of training samples. Conventional neural networks iteratively enhance neural networks based on the difference between inverted and sample P-wave impedance (Wang et al., 2020a; Wang et al., 2020b; Wang et al., 2021; Sun et al., 2021). Because the training samples are primarily created by well-log data, based on sufficient training

* Corresponding author. CNPC Key Laboratory of Geophysical Prospecting and State Key Laboratory of Petroleum Resources and Prospecting, China University of Petroleum (Beijing), Beijing, 102249, China.
E-mail address: wliuyang@vip.sina.com (Y. Liu).

https://doi.org/10.1016/j.petsci.2022.09.008

samples, neural networks can yield P-wave impedance with high resolution (Wang et al., 2019b; Xu et al., 2019a). However, in most cases, the absence of well-log data leads to the insufficiency of training samples, causing the inverted P-wave impedance to be low accuracy (Zhao et al., 2019; Wang et al., 2020c; Xu et al., 2019b).

Convolutional neural networks (CNNs) are widely employed to forecast P-wave impedance because of their weight sharing and local connection properties, which result in high feature extraction capacity (Wu et al., 2020; Yablokov et al., 2021). Nevertheless, most CNNs contain deep layers and sophisticated structures, being prone to gradient disappearance or gradient explosion, which is disadvantageous to the accuracy of inverted P-wave impedance. Residual Networks (ResNets), which are developed by adding some shortcut connections in CNNs, can solve these problems (Lin et al., 2021; Tian et al., 2021; Zhang et al., 2021).

There are always sufficient seismic data but insufficient well-log data, yielding proper initial models but insufficient training samples for field data. To balance the accuracy and the resolution of inverted P-wave impedance, we combine the advantages of model-driven and data-driven inversion methods and propose a model-data-driven P-wave impedance inversion method using ResNets, which consists of two steps, i.e., network pre-training and network retraining/inversion. During the first step, we iteratively improve the neural networks based on not only the errors between synthetic and sample seismic data but also the error between inverted and sample P-wave impedance. During the second step, we iteratively update the weight parameters of the pre-trained neural networks based on both the errors between synthetic and real seismic data and the error between the inverted P-wave impedance after low-frequency-pass filtering and the P-wave impedance of the initial model. Furthermore, because of the waveform characteristics of seismic data, the errors of seismic data calculated by the L2-norm are easily plunged into a local minimum in the iteration process if there are obvious amplitude differences (Liu et al., 2017). We introduce the normalized zero-lag cross-correlation, which can mitigate falling into a local minimum and suppress random noise, to calculate the errors. Using synthetic and field data, we evaluate the feasibility and the practicability of the proposed method and draw some useful conclusions.

2. Methods

2.1. Model-driven inversion

The foundation of most model-driven P-wave impedance inversion methods is the Robinson convolution model (Robinson, 1967) and it is shown in Appendix A. On basis of known seismic data and wavelets, most model-driven methods improve parameter models iteratively based on the differences between synthetic and real seismic data. Therefore, the objective function of a model-driven method, as calculated by the L2-norm, is depicted as

$$J_1 = \|\mathbf{S} - \mathbf{R}*\mathbf{W}\|_2, \tag{1}$$

where **S**, **R** and **W** represent seismic data, reflection coefficients, and wavelets, respectively. $\|\|_2$ stands for the L2-norm.

2.2. Data-driven inversion

Conventional data-driven inversion methods typically use neural networks to transform seismic data to P-wave impedance. By using the training samples created by well-log data, these methods usually improve the constructed neural networks iteratively based on the difference between inversion and sample P-wave impedance. As a result, the objective function, as defined by the L2-norm, is represented by

$$J_2 = \left\|\mathbf{Z}_{\mathrm{NN}} - \mathbf{Z}_{\mathrm{Sample}}\right\|_2, \tag{2}$$

where $\mathbf{Z}_{\mathrm{NN}}$ is the P-wave impedance outputted from networks and $\mathbf{Z}_{\mathrm{Sample}}$ means the sample P-wave impedance.

2.3. Model-data-driven inversion

To obtain P-wave impedance with satisfactory accuracy and resolution, we propose a model-data-driven P-wave impedance inversion method with two steps, as shown in Fig. 1.

Before the first step, the P-wave impedance low-frequency initial model for synthetic data is obtained by filtering the real P-wave impedance, while the initial model for field data is built by the seismic-structure-guided interpolation method (Wu, 2017), respectively. Meanwhile, the training samples are created by well-log data, which are augmented by adding random numbers, and seismic data, which are obtained based on the Robinson convolution model. Note that it is necessary to normalize the training samples, and we use the normalized expression as

$$\widehat{x}_j = \frac{x_j - x_{\min}}{x_{\max} - x_{\min}}, \tag{3}$$

where x_j and $\widehat{x}_j$ are the original and the normalized values of the jth sample. $x_{\max}$ and $x_{\min}$ indicate the maximum and the minimum of the samples, respectively.

The first step is network pre-training, in which we pre-train the constructed neural networks using training samples. 1D sample seismic data are fed into the neural networks to output 1D P-wave impedance that matches the 1D sample P-wave impedance. The output P-wave impedance is then used to convolute with a seismic wavelet to synthesize seismic data that are matched with the sample seismic data. In this way, the objective function in this step has two parts and is written as

$$J_3 = \mu_1 \left\|\mathbf{Z}_{\mathrm{NN}} - \mathbf{Z}_{\mathrm{Sample}}\right\|_2 + c\cdot(1-\mu_1)\left\|\mathbf{S}_{\mathrm{Syn}} - \mathbf{S}_{\mathrm{Sample}}\right\|_2, \tag{4}$$

where $\mathbf{S}_{\mathrm{Syn}}$ and $\mathbf{S}_{\mathrm{Sample}}$ are the synthetic and the sample seismic data, respectively. μ_1 represents a weight parameter with the range from 0 to 1. This parameter increases as the quality of the initial model becomes better. In this paper, we determine μ_1 as 0.5 for both the synthetic and the field data examples by test. c indicates a parameter that is used to balance the orders of magnitude and is defined as the order of magnitude of the ratio of the first term to the second term. The objective function is calculated to iteratively update the neural network weight parameters until it converges to the minimum.

The second step is network retraining/inversion, in which we update the weight parameters of the neural networks after pre-training trace by trace to obtain P-wave impedance. At first, 1D real seismic data are input into the pre-trained networks to output P-wave impedance, which is then filtered to obtain a low-frequency component with the same frequency bandwidth as the initial model. After that, the low-frequency component is constrained by the initial P-wave impedance, which will slightly lower the resolution of the inverted impedance. Meanwhile, the inverted P-wave impedance is used to calculate reflection coefficients, which then are convoluted with a statistical wavelet to synthesize seismic data to match the real seismic data. The objective function of this step also contains two parts and is defined as

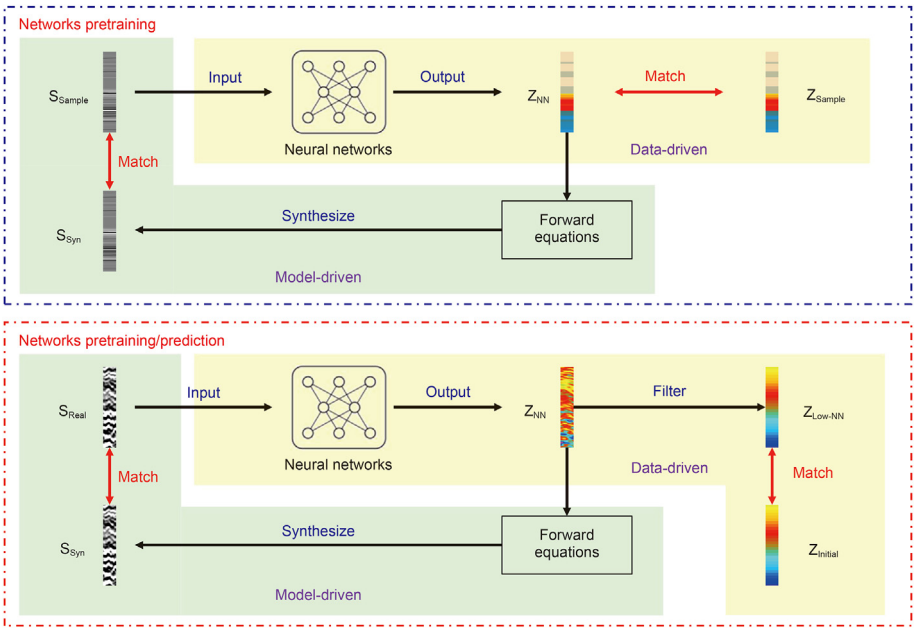

Fig. 1. The flowchart of the proposed model-data-driven inversion method.

$$J_4 = \mu_2 \|\mathbf{Z}_{\text{Low-NN}} - \mathbf{Z}_{\text{Initial}}\|_2 + c\cdot(1-\mu_2)\|\mathbf{S}_{\text{Syn}} - \mathbf{S}_{\text{Real}}\|_2, \tag{5}$$

where $\mathbf{Z}_{\text{Low-NN}}$ represents the inversion P-wave impedance after low-frequency filtering and $\mathbf{Z}_{\text{Initial}}$ indicates the initial P-wave impedance. $\mathbf{S}_{\text{Real}}$ is the real seismic data. μ_2 denotes a weight parameter (ranging from 0 to 1) that increases in size as the initial model is enhanced. The more proper the initial model is, the bigger μ_2 is, and the higher the dependence of the proposed method on the initial model is. In this paper, we determine μ_2 as 0.5 for the synthetic data example and 0.3 for the field data example by test. The objective function is calculated to iteratively update the pre-trained neural networks trace by trace until it converges to the minimum, and the P-wave impedance output from the networks is the inversion parameter.

The first items on the right side of Eqs. (4) and (5) show P-wave impedance constraints that are affected by the training samples and initial model, respectively. The second items on the right side of Eqs. (4) and (5) represent the constraints of seismic data. Because seismic data have waveform characteristics, the L2-norm objective function, which requires amplitude matching, is prone to falling into a local minimum and yielding low accuracy when there are amplitude differences between synthetic and real seismic data. The normalized zero-lag cross-correlation objective function can effectively process such amplitude differences by matching the phase between waveforms. Furthermore, the objective function reduces the importance of amplitude and is insensitive to random noise in seismic data, which can effectively decrease the influence of the random noise on inversion (Liu et al., 2017). By using the normalized zero-lag cross-correlation, the proposed method improves the objective functions used in the network pre-training and network retraining/inversion steps as

$$J_5 = \mu_1 \left\|\mathbf{Z}_{\text{NN}} - \mathbf{Z}_{\text{Sample}}\right\|_2 + c\cdot(1-\mu_1)\left(1 - \frac{S_{\text{NN}}\cdot S_{\text{Sample}}}{\sqrt{S_{\text{NN}}^2}\cdot\sqrt{S_{\text{Sample}}^2}}\right), \tag{6}$$

and

$$J_6 = \mu_2 \|\mathbf{Z}_{\text{Low-NN}} - \mathbf{Z}_{\text{Initial}}\|_2 + c\cdot(1-\mu_2)\left(1 - \frac{S_{\text{NN}}\cdot S_{\text{Real}}}{\sqrt{S_{\text{NN}}^2}\cdot\sqrt{S_{\text{Real}}^2}}\right), \tag{7}$$

By learning from Wu's neural networks (Wu et al., 2021), the proposed method employs ResNets (shown in Fig. 2), which contain four convolution layers and four ResBlocks. Each convolution layer is composed of 16 1D convolution filters and is followed by a ResBlock (shown in the green box), which includes two convolution layers and a skip connection over the two layers. We use the ReLU activation function to add nonlinear information and apply the Adam optimization algorithm to enhance the weight parameters of neural networks by minimizing the objective functions with the learning rate of 0.001.

3. Examples

To test the feasibility and the progressiveness of the proposed model-data-driven method, we compare it with a model-driven inversion method based on the least square algorithm and a data-driven inversion method using the ResNets depicted in Fig. 2. We use these three methods to process synthetic and field data for the trial. Besides, the mean squared error (MSE) and the running time are used to evaluate these three methods. The MSE's expression is written as

$$\text{MSE} = \frac{1}{n}\sum_{i=1}^{n}(m_i - m_i')^2, \tag{8}$$

where m and m' mean inverted and real data, respectively. n is the number of m.

3.1. Synthetic data example

As synthetic data, 401 CDPs (common depth points) and 501

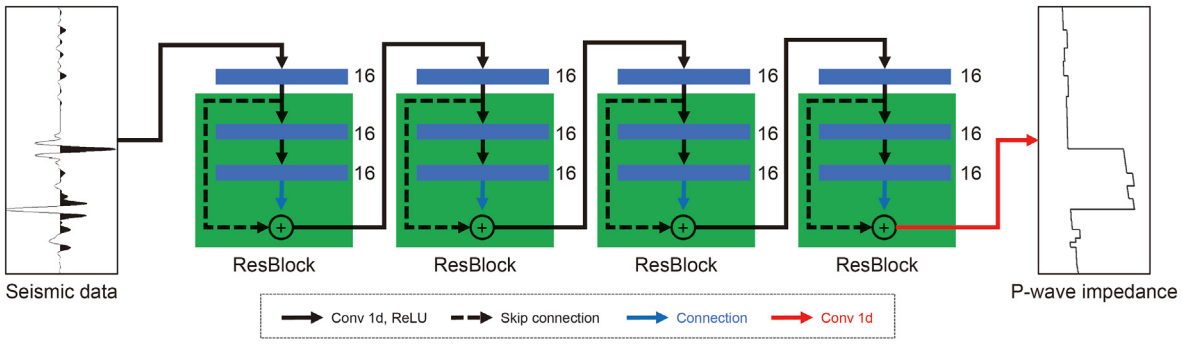

Fig. 2. The structure of the ResNets used in the proposed method.

samples with a 2 ms interval from the Marmousi model are used. The real P-wave impedance of the partial Marmousi model (shown in Fig. 3a) is used to calculate reflection coefficients, which are then applied to convolute with a Ricker wavelet with the dominant frequency of 20 Hz (shown in Fig. 3b) to synthesize real seismic data without noise (displayed in Fig. 3c). The data of real P-wave impedance's 101th, 201th, and 301th CDPs are used to establish pseudo wells, which are then named as Wells 1, 2, and 3. We build an initial model by filtering the real P-wave impedance, as drawn in Fig. 3d. Meanwhile, the P-wave impedances of Wells 1 and 2 are augmented by adding random numbers and then are applied to compute seismic data based on the Robinson convolution model. In this way, we create 1000 training samples to train the neural networks for the synthetic data example. The well-log data of Well 3 are used for verification.

By using the initial model shown in Fig. 3d, the model-driven method inverts the real seismic data without noise and provides the P-wave impedance shown in Fig. 4a. Fig. 4b depicts the P-wave impedance inverted by the data-driven method after 300 epochs based on the training samples. Meanwhile, by employing both the initial model and the training samples, the proposed model-data-driven method deduces the P-wave impedance displayed in Fig. 3c after 300 epochs for the pre-training step. One can see that the P-wave impedance inverted by the model-driven method has a lower resolution than those of both the data-driven and the proposed model-data-driven methods.

To clearly show the differences of the P-wave impedances inverted by these three methods, we extract the data of Wells 1 and 3 and show them in Fig. 5a and b, respectively. One can see that the P-wave impedances inverted by the proposed method are closer to the well-log data than the impedances obtained by the model-driven method for these two wells. The data-driven method provides the P-wave impedances that match the well-log data well only for Well 1. Meanwhile, the MSEs of these inverted P-wave impedances are calculated and then displayed in Fig. 6a and b. For Well 1, whose data are used to create training samples, the model-driven, the data-driven, and the proposed methods provide the MSEs with 0.253, 0.180, and 0.173, respectively. For Well 3, which is a validation well, these three methods invert P-wave impedances with the MSEs of 0.257, 0.411, and 0.181. Our proposed method deduces the impedances with the lowest MSEs and the highest accuracy for both the two wells.

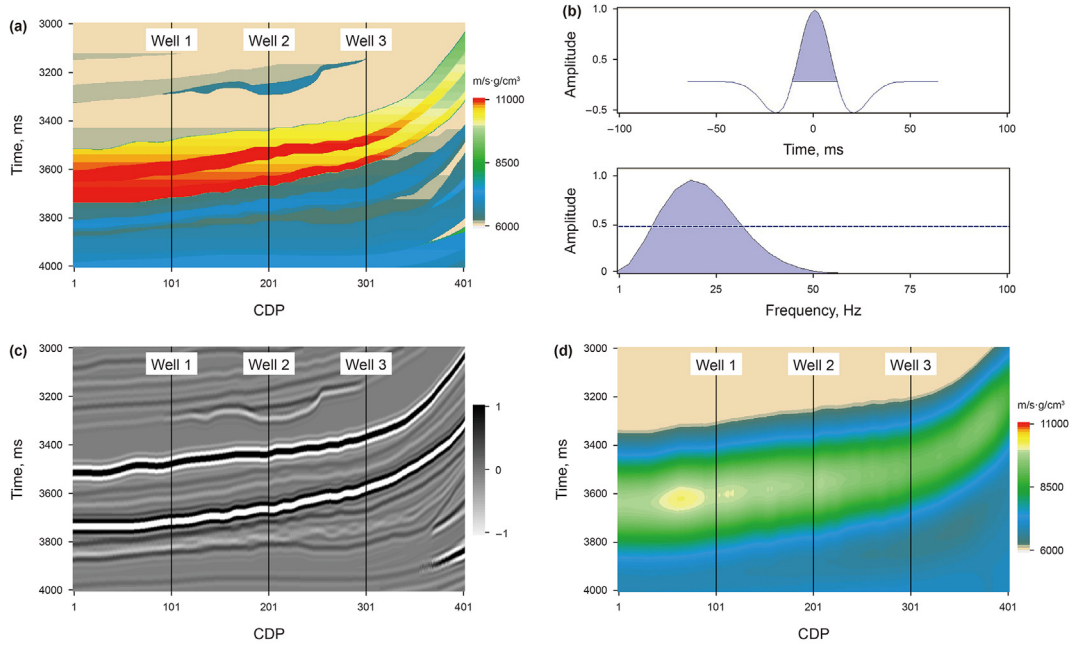

Fig. 3. Test on the synthetic seismic data without noise for the partial Marmousi model. (a) Real P-wave impedance. (b) Ricker wavelet with the dominant frequency of 20 Hz. (c) Synthetic seismic data without noise. (d) P-wave impedance low-frequency initial model.

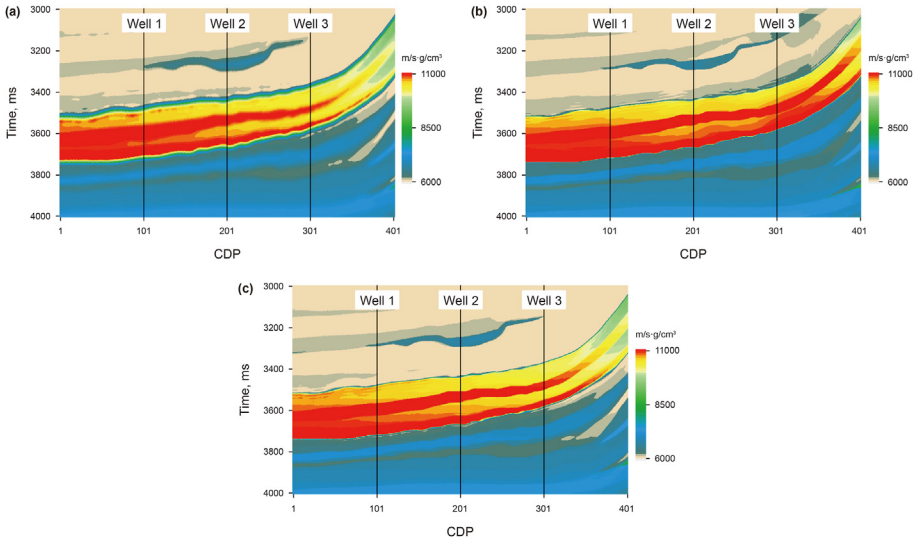

Fig. 4. Test on the synthetic seismic data without noise for the partial Marmousi model. (a, b, and c) P-wave impedances inverted by the model-driven, the data-driven, and the proposed model-data-driven methods.

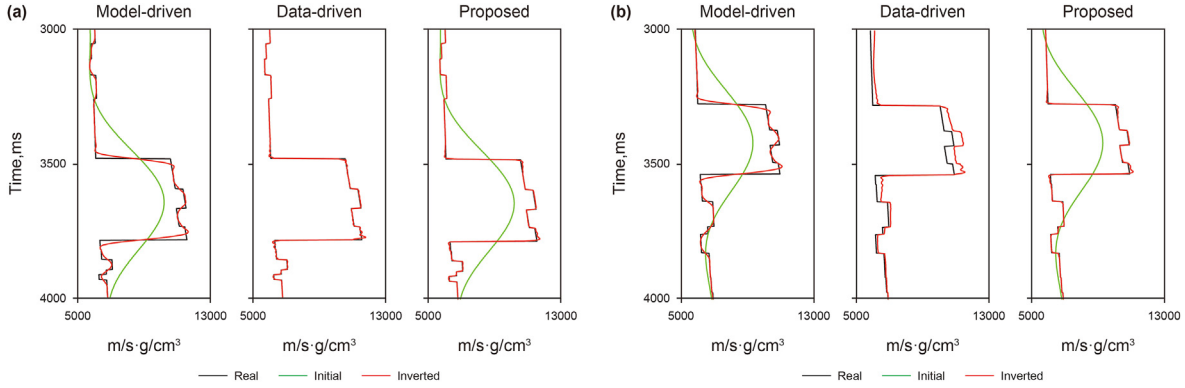

Fig. 5. Test on synthetic seismic data without noise for the partial Marmousi model. (a) Well-log, initial and inverted P-wave impedances of Well 1. (b) Well-log, initial and inverted P-wave impedances of Well 3.

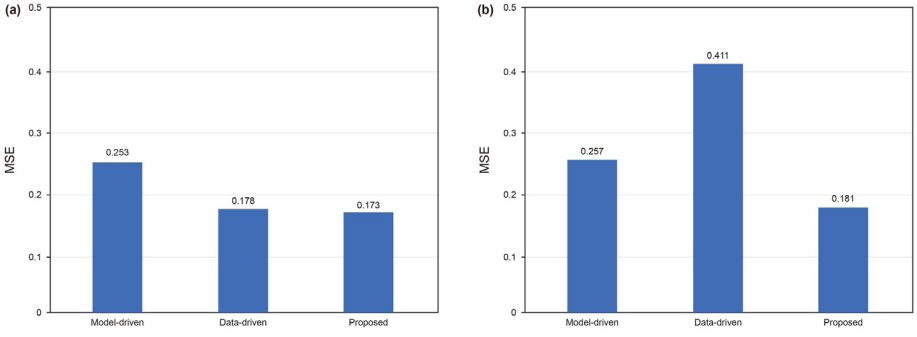

Fig. 6. Test on the synthetic seismic data without noise for the partial Marmousi model. (a) The MSEs of the P-wave impedances inverted by the three methods for Well 1. (b) The MSEs of the P-wave impedances inverted by the three methods for Well 3.

Table 1 shows the running time of the three methods. The model-driven method takes the shortest time to obtain the inverted P-wave impedance shown in Fig. 4, while the proposed method takes the longest time, which is still acceptable.

In addition, to test the anti-noise ability of the proposed method, we add some random noise in the noiseless seismic data to obtain noisy seismic data with the signal-to-noise ratio of 2 (shown in Fig. 7a). The model-data-driven methods, which employ the L2 norm objective function (Eq. (4) and (5)) and the normalized zero-lag cross-correlation objective function (Eq. (6) and (7)), are used to process the noisy seismic data and invert the P-wave impedances depicted in Fig. 7b and c. For clarity, Fig. 8a and b shows the curves of the initial model, the inverted P-wave impedances, and the well-log data from Wells 1 and 3. One can see that the P-wave

Table 1
The running time of the three methods for the synthetic seismic data without noise.

Methods		Pre-training (s)	Retraining/Inversion (s)	Total (s)
Model-driven	Initial model	–	40	40
Data-driven	Train samples	85	–	85
Proposed	Initial model+ Train samples	107	48	155

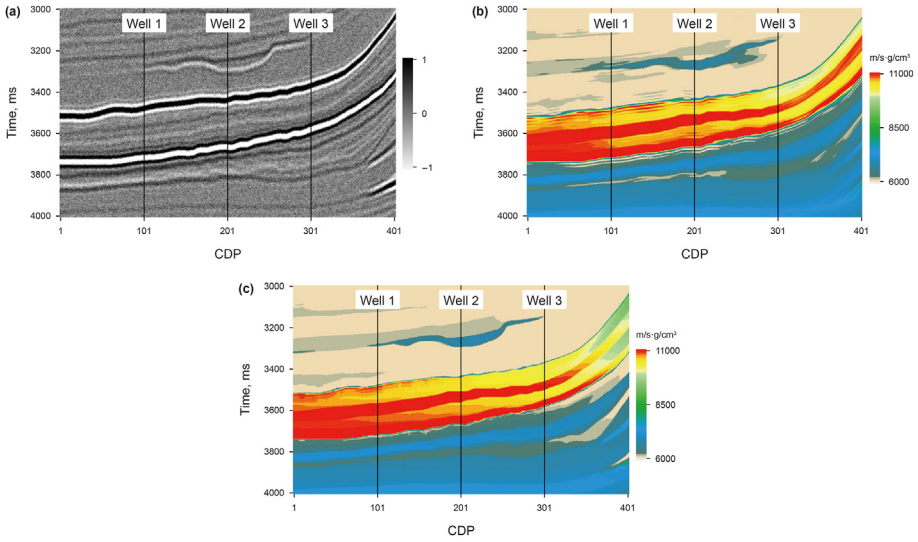

Fig. 7. Test on the synthetic seismic data with noise for the partial Marmousi model. (a) Synthetic seismic data with noise. (b and c) P-wave impedances inverted by the proposed model-data-driven methods based on the L2-norm and the normalized zero-lag cross-correlation objective functions, respectively.

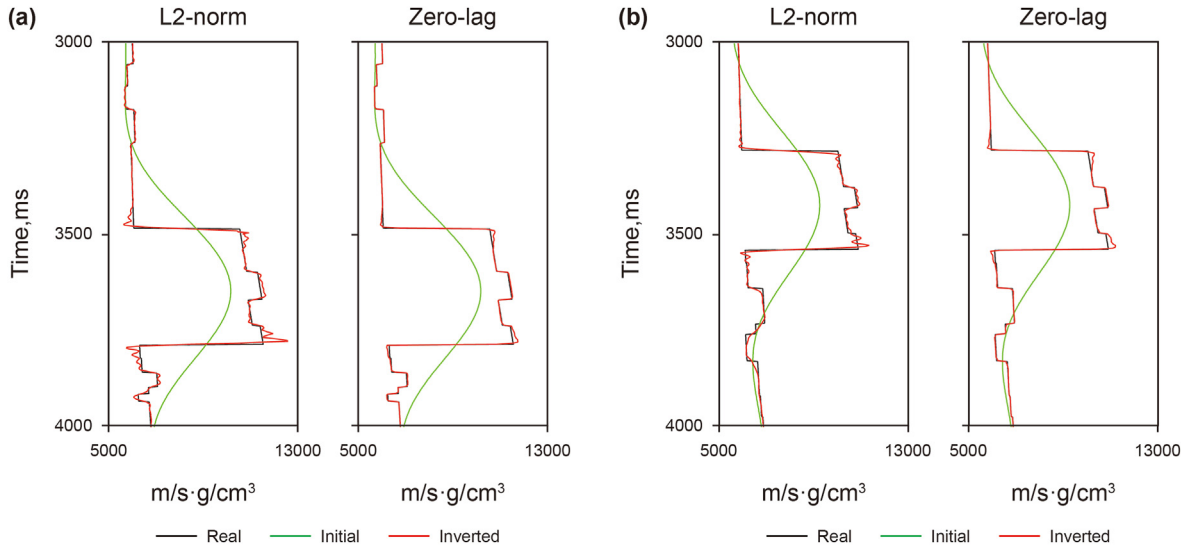

Fig. 8. Test on the synthetic seismic data with noise for the partial Marmousi model. (a) Well-log, initial and inverted P-wave impedances of Well 1. (b) Well-log, initial and inverted P-wave impedances of Well 3.

impedances inverted based on the normalized zero-lag cross-correlation objective function (the MSEs are 0.175 and 0.182, respectively) match the well-log data better than those of the L2-norm objective function (the MSEs are 0.208 and 0.213, respectively). It demonstrates that the normalized zero-lag cross-correlation objective function has benefits of anti-noise.

3.2. Field data example

The field data, consisting of 900 inline and 400 Xline, contain 250 samples with an interval of 2 ms. Fig. 9a shows the 3D field seismic data and 4 wells. We extract the statistical wavelet (displayed in Fig. 9b) from the seismic data for inversion and build the P-wave impedance initial model (revealed in Fig. 9c) based on the seismic-structure-guided interpolation method (Wu, 2017). After

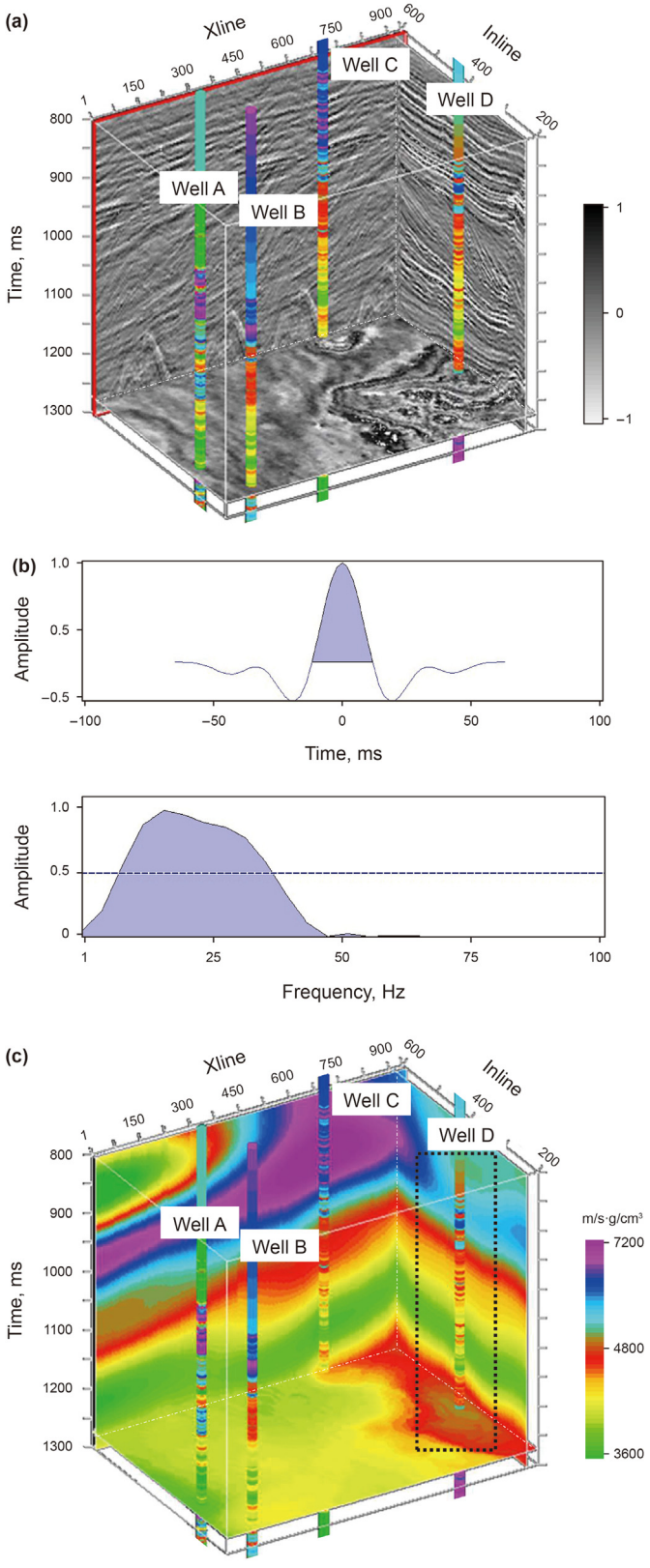

Fig. 9. Test on the field seismic data. (a) 3D field seismic data. (b) A statistical wavelet extracted from the seismic data. (c) P-wave impedance low-frequency initial model.

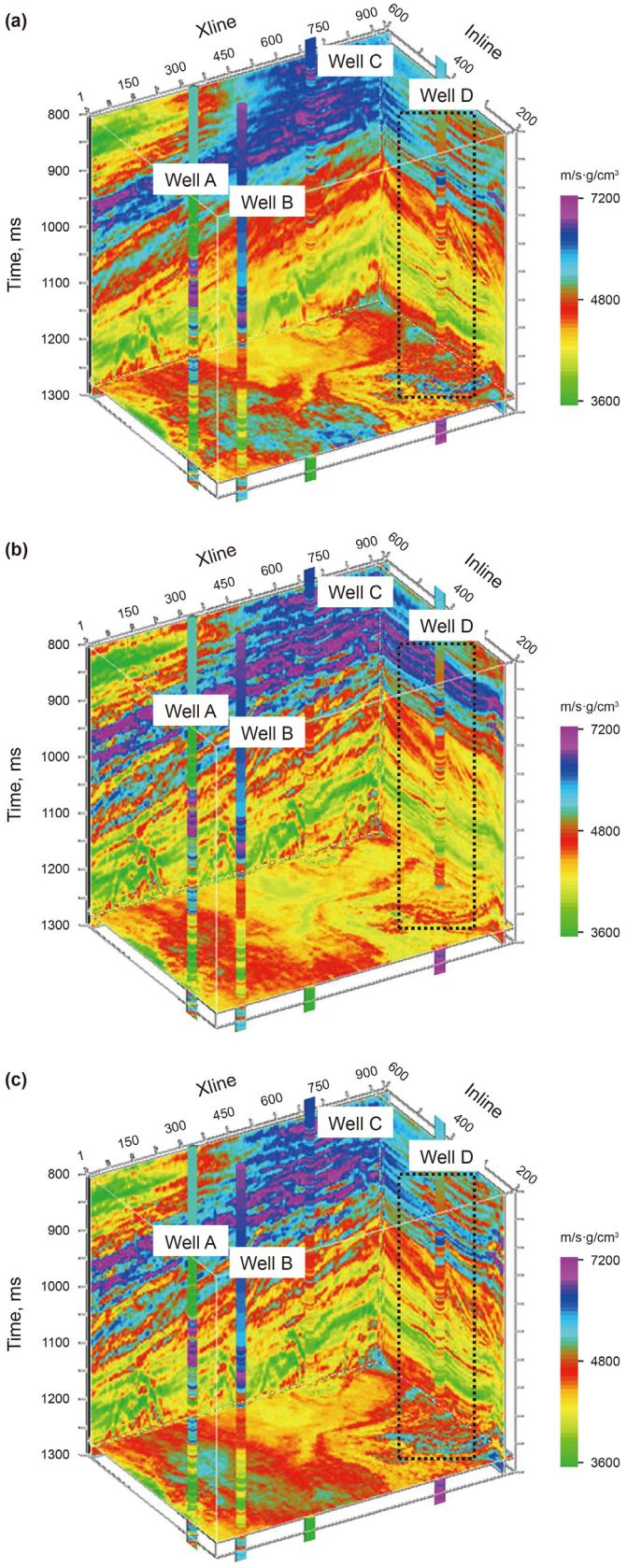

Fig. 10. Test on the field seismic data. (a, b, and c) P-wave impedances inverted by the model-driven, the data-driven, and the proposed model-data-driven methods.

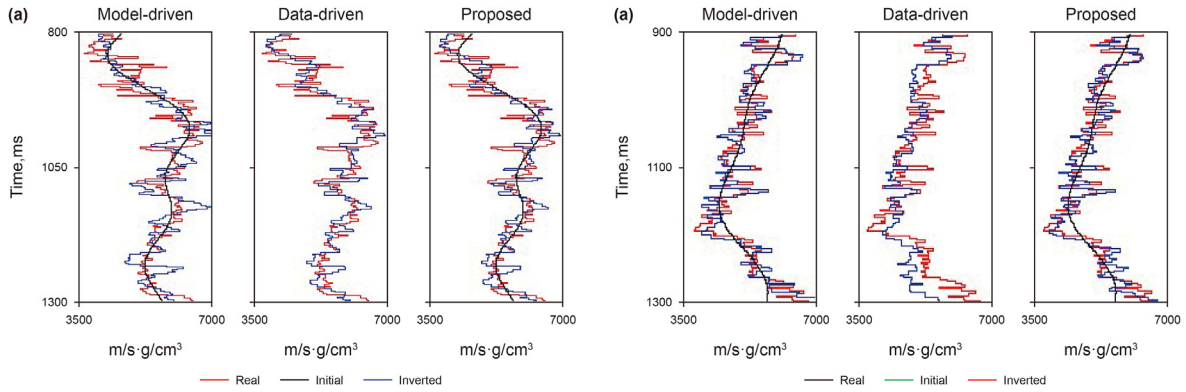

Fig. 11. Test on the field seismic data. (a) Well-log, initial, and inverted P-wave impedances of Well A. (b) Well-log, initial, and inverted P-wave impedances of Well D.

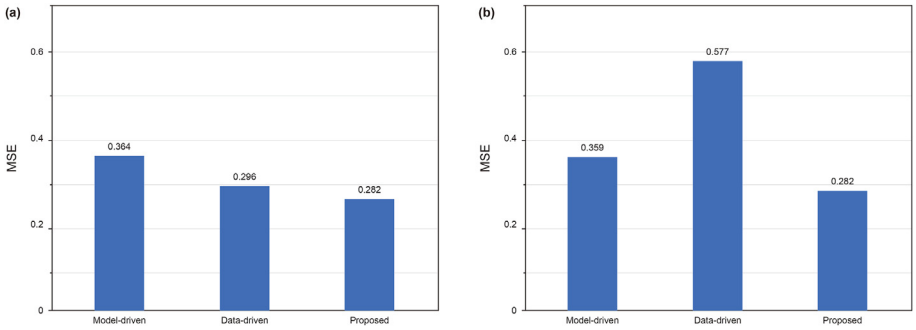

Fig. 12. Test on the field seismic data. (a) The MSEs of the P-wave impedances inverted by the three methods for Well A. (b) The MSEs of the P-wave impedances inverted by the three methods for Well D.

that, we create 5000 training datasets using the sample generation method mentioned in the synthetic data example based on the well-log data of Wells A, B, and C. The P-wave impedance of Well D is used as the validation data.

The model-driven method inverts the field seismic data based on the initial model and generates the P-wave impedance shown in Fig. 10a. Fig. 10b displays the P-wave impedance inverted by the data-driven method using the training samples after 300 epochs. Meanwhile, the proposed model-data-driven method with the zero-lag cross-correlation-based functions employs both the initial model and the training samples and obtains the P-wave impedance revealed in Fig. 10c by costing 300 epochs in the pre-training step. It can be seen that the P-wave impedances inverted by the data-driven and the proposed methods have higher resolution than that of the model-driven method, especially around the Well C.

Fig. 11 shows the P-wave impedances of Wells A and D for clear comparisons. Concurrently, the MSEs of inverted impedances of these two wells are calculated and drawn in Fig. 12a and b, respectively. One can see that the model-driven, the data-driven, and the proposed methods invert the P-wave impedances with the MSEs of 0.364, 0.296, and 0.267, respectively for Well A. It demonstrates that the proposed method provides the impedance with the highest accuracy among the three methods. Meanwhile, the MSEs of P-wave impedances inverted by the three methods are 0.359, 0.577, and 0.282 for Well D (shown in the black dashed boxes in Fig. 10). It indicates that the data-driven method cannot provide high accuracy impedance if there are insufficient training samples while the proposed method can still invert the P-wave impedance with high accuracy.

4. Conclusions

We proposed a model-data-driven method to invert P-wave impedance using ResNets and the normalized zero-lag cross-correlation objective function. Based on the same initial model, the proposed model-data-driven method can provide the P-wave impedance with both higher accuracy and higher resolution than that of the model-driven method because our method uses additional training samples. Using the same training samples, the proposed method outperforms the data-driven method in terms of P-wave impedance accuracy because it employs an additional initial model. Meanwhile, the proposed method performs well in anti-noise for using the normalized zero-lag cross-correlation objective function. This paper primarily advances a feasible inversion strategy that combines model-driven and data-driven methods by utilizing simple neural networks. When more appropriate networks are built, the new method will provide a more satisfactory P-wave impedance.

Note that the model-driven method efficiently inverts P-wave impedance with high accuracy but limited resolution. The data-driven method provides P-wave impedance with both high resolution and accuracy only around wells or in locations, whose characteristics are similar to well-log data. But these methods have higher efficiency than the proposed model-data-driven method. As a result, we suggest that the model-driven methods are suitable to invert the seismic data with a broad frequency bandwidth. The data-driven methods are good at processing the field data, which contain sufficient wells or training samples. Our proposed model-data-driven method can perform better than these two methods when seismic data have low resolution and well-log data are insufficient.

Acknowledgments

This research is financially supported by the Important National Science & Technology Specific Project of China (Grant No. 2017ZX05018-005).

Appendix A

The Robinson convolution model theory (Robinson, 1967) is expressed mathematically as

$$\mathbf{S} = \mathbf{R} * \mathbf{W}, \tag{A.1}$$

where **S**, **R** and **W** represent seismic data, reflection coefficients, and wavelets, respectively.

When seismic waves propagate to an underground reflection interface vertically, the reflection coefficient at the interface is defined as

$$R_i = \frac{Z_{i+1} - Z_i}{Z_{i+1} + Z_i}, \tag{A.2}$$

where R_i is the reflection coefficient at the interface, Z_i and Z_{i+1} indicate the P-wave impedances above and below the interface, respectively.

References

Ajaz, M., Ouyang, F., Wang, G.H., et al., 2021. Fluid identification and effective fracture prediction based on frequency-dependent AVOAz inversion for fractured reservoirs. Petrol. Sci. 18 (4), 1069–1085. https://doi.org/10.1016/j.petsci.2021.07.011.

Alfarraj, M., AlRegib, G., 2019. Semi-supervised Learning for Acoustic Impedance Inversion. 89th Annual International Meeting. SEG Expanded Abstracts, pp. 2298–2302. https://doi.org/10.1190/segam2019-3215902.1.

Baeten, G., Maag, J.W., Plessix, R.E., et al., 2013. The use of low frequencies in a full-waveform inversion and impedance inversion land seismic case study. Geophys. Prospect. 61 (4), 701–711. https://doi.org/10.1111/1365-2478.12010.

Biswas, R., Sen, M.K., Das, V., et al., 2019. Prestack and poststack inversion using a physics-guided convolutional neural network. Interpretation 7 (3), SE161–SE174. https://doi.org/10.1190/INT-2018-0236.1.

Chen, T.S., Innanen, K.A., 2014. AVO inversion through iteration of direct nonlinear inverse formulas. CREWES Research Report 26, 1–16.

Chen, Y.Q., Schuster, G.T., 2020. Seismic inversion by Newtonian machine learning. Geophysics 85 (4), WA185–WA200. https://doi.org/10.1190/geo2019-0434.1.

Cheng, G.S., Yin, X.Y., Zong, Z.Y., et al., 2021a. Complex spherical-wave elastic inversion using amplitude and phase reflection information. Petrol. Sci. https://doi.org/10.1016/j.petsci.2021.12.005.

Cheng, J.W., Zhang, F., Li, X.Y., 2021b. Nonlinear amplitude inversion using a hybrid quantum genetic algorithm and the exact Zoeppritz equation. Petrol. Sci. https://doi.org/10.1016/j.petsci.2021.12.014.

Dai, R.H., Yin, C., Yang, S.S., et al., 2018. Seismic deconvolution and inversion with erratic data. Geophys. Prospect. 66 (9), 1684–1701. https://doi.org/10.1111/1365-2478.12689.

Das, V., Pollack, A., Wollner, U., et al., 2019. Convolutional neural network for seismic impedance inversion. Geophysics 84 (6), R869–R880. https://doi.org/10.1190/geo2018-0838.1.

Guo, R., Zhang, J.J., Liu, D., et al., 2019. Application of Bi-directional Long Short-Term Memory Recurrent Neural Network for Seismic Impedance Inversion. 81st Conference and Exhibition, vols. 3–6. EAGE Extended Abstracts. https://doi.org/10.3997/2214-4609.201901386.

Hu, G.Q., Liu, Y., Wei, X.C., et al., 2011. Joint PP and PS AVO inversion based on Bayes theorem. Appl. Geophys. 8 (4), 293–302. https://doi.org/10.1007/s11770-010-0306-0.

Innanen, K.A., 2011. Inversion of the seismic AVF/AVA signatures of highly attenuative targets. Geophysics 76 (1), R1–R11. https://doi.org/10.1190/1.3518816.

Kieu, D.T., Kepic, A., 2019. Seismic-impedance inversion with fuzzy clustering constraints: an example from the Carlin Gold District, Nevada, USA. Geophys. Prospect. 68 (1), 103–128. https://doi.org/10.1111/1365-2478.12891.

Li, Y.Q., Li, J.Y., Chen, X.H., et al., 2020. Post-stack impedance blocky inversion based on analytic solution of viscous acoustic wave equation. Geophys. Prospect. 68 (7), 2009–2026. https://doi.org/10.1111/1365-2478.12967.

Lin, B.H., Jin, X., Kang, L.C., et al., 2021. The research of earthquake magnitude determination based on convolution neural networks. Chin. J. Geophys. 64 (10), 3600–3611. https://doi.org/10.6038/cjg2021O0370 (in Chinese).

Liu, Y.S., Teng, J.W., Xu, T., et al., 2017. Robust time-domain full waveform inversion with normalized zero-lag cross-correlation objective function. Geophys. J. Int. 209 (1), 106–122. https://doi.org/10.1093/gji/ggw485.

Lu, J., Yang, Z., Wang, Y., et al., 2015. Joint PP and PS AVA seismic inversion using exact Zoeppritz equations. Geophysics 80 (5), R239–R250. https://doi.org/10.1190/geo2014-0490.1.

Ma, M., Zhang, R., Yuan, S.Y., 2019. Multichannel impedance inversion for nonstationary seismic data based on the modified alternating direction method of multipliers. Geophysics 84 (1), A1–A6. https://doi.org/10.1190/geo2018-0319.1.

Ma, X., Huo, L.L., Li, G.F., et al., 2021. Inversion-based attenuation compensation with dip constraint. Petrol. Sci. https://doi.org/10.1016/j.petsci.2021.12.001.

Puzyrev, V., Egorov, A., Pirogova, A., et al., 2019. Seismic inversion with deep neural networks: a feasibility analysis. In: 81st Annual International Meeting, vols. 3–6. EAGE Expanded Abstracts. https://doi.org/10.3997/2214-4609.201900765.

Robinson, E.A., 1967. Predictive decomposition of time series with application to seismic exploration. Geophysics 32, 418–484. https://doi.org/10.1190/1.1439873.

Shi, L., Sun, Y.H., Liu, Y., et al., 2020. High-order AVO inversion for effective pore-fluid bulk modulus based on series reversion and Bayesian theory. Energies 13 (6), 1313. https://doi.org/10.3390/en13061313.

Sun, Y.H., Liu, Y., Chen, T.S., 2021. Multi-wave amplitude-versus-offset inversion and reservoir fluid identification based on unsupervised deep learning. Geophys. Prospect. Pet. 60 (3), 385–394. https://doi.org/10.3969/j.issn.1000-1441.2021.03.004 (in Chinese).

Tian, Y.J., Gao, J.H., Wang, D.Q., et al., 2021. Removing strong seismic reflection based on the deep neural network. Chin. J. Geophys. 64 (8), 2780–2794. https://doi.org/10.6038/cjg2021O0165 (in Chinese).

Wang, Y.Q., Ge, Q., Lu, W., et al., 2020c. Well-logging constrained seismic inversion based on closed-loop convolutional neural network. IEEE Trans. Geosci. Rem. Sens. 58 (8), 5564–5574. https://doi.org/10.1109/TGRS.2020.2967344.

Wang, N., Xing, G., Zhu, T., Zhou, H., et al., 2022. Propagating seismic waves in VTI attenuating media using fractional viscoelastic wave equation. J. Geophys. Res. Solid Earth 127. https://doi.org/10.1029/2021JB023280.

Wang, E.J., Liu, Y., Ji, Y.X., et al., 2019a. Q full-waveform inversion based on the viscoacoustic equation. Appl. Geophys. 16 (1), 77–91. https://doi.org/10.1007/s11770-019-0749-2.

Wang, Y.Q., Lu, W.K., Liu, J.L., et al., 2019b. Random seismic noise attenuation based on data augmentation and CNN. Chin. J. Geophys. 62 (1), 421–433. https://doi.org/10.6038/cjg2019M0385 (in Chinese).

Wang, L.L., Meng, D.L., Wu, B.Y., 2020a. Seismic inversion via closed-loop fully convolutional residual network and transfer learning. Geophysics 86 (5), 1–54. https://doi.org/10.1190/geo2020-0297.1.

Wang, Y.Q., Wang, Q., Lu, W.K., et al., 2021. Seismic impedance inversion based on cycle-consistent generative adversarial network. Petrol. Sci. https://doi.org/10.1016/j.petsci.2021.09.038.

Wang, W.B., Xu, X.L., Sheng, L., et al., 2020b. Detection of microseismic events based on convolution neural networks. Oil Geophys. Prospect. 55 (5), 939–949 (in Chinese). http://www.ogp-cn.com/EN/10.13810/j.cnki.issn.1000-7210.2020.05.001.

Wu, X.M., 2017. Building 3D subsurface model conforming to seismic structural and stratigraphic features. Geophysics 82 (3), IM21–IM30. https://doi.org/10.1016/j.petsci.2021.09.038.

Wu, B., Meng, D., Wang, L.L., et al., 2020. Seismic impedance inversion using fully convolutional residual network and transfer learning. Geosci. Rem. Sens. Lett. IEEE 17 (12), 2140–2144. https://doi.org/10.1109/LGRS.2019.2963106.

Wu, X.M., Yan, S.S., Bi, Z.F., et al., 2021. Deep learning for multidimensional seismic impedance inversion. Geophysics 86 (5), R735–R745. https://doi.org/10.1190/geo2020-0564.1.

Xu, P., Lu, W., Tang, J., et al., 2019a. High-resolution reservoir prediction using convolutional neural networks. In: 81st Annual International Meeting, vols. 1–5. EAGE Expanded Abstracts. https://doi.org/10.3997/2214-4609.201901392.

Xu, P., Lu, W., Wang, B., 2019b. A semi-supervised learning framework for gas chimney detection based on sparse auto encoder and TSVM. J. Geophys. Eng. 16 (1), 52–61. https://doi.org/10.1093/jge/gxy004.

Yablokov, A.V., Serdyukov, A.S., Loginov, G.N., et al., 2021. An artificial neural network approach for the inversion of surface wave dispersion curves. Geophys. Prospect. 69 (7), 1405–1432. https://doi.org/10.1111/1365-2478.13107.

Yin, X.Y., Zhang, S.X., 2014. Bayesian inversion for effective pore-fluid bulk modulus based on fluid-matrix decoupled amplitude variation with offset approximation. Geophysics 79 (5), R221–R232. https://doi.org/10.1190/geo2013-0372.1.

Zhang, Y.L., Yu, Z.C., Hu, T.Y., et al., 2021. Multi-trace joint downhole microseismic phase detection and arrival picking method based on U-net. Chin. J. Geophys. 64 (6), 2073–2085. https://doi.org/10.6038/cjg2021O0379 (in Chinese).

Zhao, M., Chen, S., Fang, L.H., et al., 2019. Earthquake phase arrival auto-picking based on U-shaped convolution neural networks. Chin. J. Geophys. 62 (8), 3034–3042. https://doi.org/10.6038/cjg2019M0495 (in Chinese).

Zhou, D.Y., Yin, X.Y., Zong, Z.Y., 2019. Multi-trace basis-pursuit seismic inversion for resolution enhancement. Geophys. Prospect. 67 (3), 519–531. https://doi.org/10.1111/1365-2478.12752.

Zhou, L., Li, J.Y., Chen, X.H., et al., 2017. Prestack amplitude versus angle inversion for Young's modulus and Poisson's ratio based on the exact Zoeppritz equations. Geophys. Prospect. 65 (6), 1462–1476. https://doi.org/10.1111/1365-2478.12493.